International Journal of
Molecular Sciences

MDPI

Article

Enhanced Photocatalytic Activity of Anatase/Rutile Heterojunctions by Lanthanum and Tin Co-Doping

Xiaodong Zhu [1], Fengqiu Qin [1], Lili He [1], Yu Jiao [2,*] and Wei Feng [1,*]

[1] School of Mechanical Engineering, Chengdu University, Chengdu 610106, China
[2] School of Science, Xichang University, Xichang 615013, China
* Correspondence: jiaoyu@xcc.edu.cn (Y.J.); fengwei@cdu.edu.cn (W.F.)

Abstract: Anatase/rutile heterojunctions were prepared using the sol–gel method and modified by La/Sn single doping and co-doping. Sn doping promoted the transformation from anatase to rutile, while La doping inhibited the phase transformation. La and Sn co-doping showed an inhibitory effect. The co-doping of La and Sn did not increase visible-light absorption, but exhibited a synergistic effect on inhibiting the recombination of photogenerated electrons and holes, which improved the photocatalytic activity on the basis of single-element modification. The first-order reaction rate constant of La/Sn co-doped sample was 0.027 min^{-1}, which is 1.8 times higher than that of pure TiO_2 (0.015 min^{-1}). Meanwhile, the mechanism of photodegradation of methylene blue (MB) by La/Sn co-doped anatase/rutile heterojunctions was discussed through electrochemical measurements and free-radical trapping experiments.

Keywords: anatase/rutile heterojunctions; sol–gel method; La/Sn co-doping; photocatalytic activity

Citation: Zhu, X.; Qin, F.; He, L.; Jiao, Y.; Feng, W. Enhanced Photocatalytic Activity of Anatase/Rutile Heterojunctions by Lanthanum and Tin Co-Doping. *Int. J. Mol. Sci.* **2022**, *23*, 11339. https://doi.org/10.3390/ijms231911339

Academic Editors: Jianghui Zheng, Guohua Xie and Andrea Crovetto

Received: 1 September 2022
Accepted: 20 September 2022
Published: 26 September 2022

1. Introduction

As a photocatalytic material, TiO_2 is favored in the field of photocatalytic degradation of pollutants due to its advantages of stable chemical properties, nontoxicity, low cost, availability, and reusability [1–3]. The photogenerated electrons and holes of pure TiO_2 are easily recombined, which limits its practical application. Modifying TiO_2 by ion doping can form lattice defects, change the energy band structure, inhibit the recombination of photogenerated electrons and holes, and improve the photocatalytic efficiency [4–7]. Due to the synergistic effect of different elements, the co-doping modification is known to be more efficient than single doping in enhancing the photocatalytic performances of functional materials [8–14]. Chen et al. [15] loaded Ce/N co-doped TiO_2 on diatomite, and the results showed that Ce/N co-doped sample had the smallest bandgap width because N doping made the valence band move up, and Ce doping formed an impurity level in the forbidden band, which were conducive to narrowing the bandgap width. Furthermore, the Ce/N co-doped sample showed the smallest grain size and the largest specific surface area. The activity of the co-doped sample was higher than that of the single-doped samples.

It has been reported that the photocatalytic activity of TiO_2 is improved obviously after La doping [16–19]. Nesic et al. [16] and Peng et al. [17] found that the specific surface area of TiO_2 increased after La doping, which was conducive to the photocatalytic activity. The study of Xin et al. [18] showed that La doping contributed to the increase in anatase content, the formation of the Ti–O–La bond was conducive to the improvement of adsorption performance, and the introduced O vacancies effectively inhibited the recombination of carriers, thus showing higher photocatalytic activity than pure TiO_2. On the other hand, Sn-doped TiO_2 exhibited better photocatalytic performance than pure TiO_2 [20–23]. Mohamed et al. [20] found that, after Sn doping, the specific surface area increased, the visible-light absorption significantly improved, and the recombination of photogenerated electrons and holes was inhibited, which were advantageous to the photocatalytic activity. Therefore, it is reasonable to speculate that

the La/Sn co-doping modification of TiO_2 can give play to the advantages of each element, form a synergistic effect, and achieve a better modification effect.

In this work, pure TiO_2 with anatase and rutile mixed crystal was prepared using the sol–gel method and then modified by single doping and co-doping of La and Sn elements, respectively. Pure TiO_2, Sn-doped TiO_2, La-doped TiO_2, and La/Sn co-doped TiO_2 were labeled as PT, ST, LT, and LST, respectively. The crystal structure, surface morphology, elemental composition, valence state, and optical properties of samples were analyzed, and the mechanism of improving the photocatalytic performance of co-doped TiO_2 was systematically discussed.

2. Results and Discussion

2.1. Photocatalyst Characterization

Figure 1 shows the XRD patterns of samples. The diffraction peaks of PT pattern appeared near 27.3°, 41.2°, and 44.3°, corresponding to the crystal planes of rutile (110), (111), and (210), respectively (JCPDS NO. 21-1276). The diffraction peaks of anatase (101), (004), and (200) crystal planes appeared at 25.3°, 37.8°, and 48.1° (JCPDS NO. 21-1272). The results show that PT had an anatase/rutile mixed crystalline structure. Most of the diffraction peaks corresponded to rutile phase in the ST pattern, indicating that Sn doping promoted the transformation from anatase to rutile. Correspondingly, anatase peaks could only be found in the pattern of LT, suggesting that the phase transformation was inhibited by La doping. Due to their similar ionic radius, Sn^{4+} ions (0.069 nm) could enter the lattice to replace Ti^{4+} ions (0.0605 nm), causing lattice defects, weakening the binding force between atoms, and making the Ti–O bonds easier to crack, which was conducive to phase transition [5]. Furthermore, since SnO_2 and rutile have the same crystal structure, SnO_2 would become the heterogeneous nucleation center of rutile, promoting the transformation [22]. The radius of La^{3+} ions (0.103 nm) is much larger than that of Ti^{4+} ions, hindering their entry into the TiO_2 lattice. La elements should be dispersed on the surface of TiO_2 particles in the form of oxide La_2O_3 [6]. The transformation requires the rearrangement of atoms and the breaking of bonds. La_2O_3 dispersed on TiO_2 surface will hinder the migration of Ti and O atoms, and delay the nucleation and growth of rutile, inhibiting the phase transition [6,19]. It can be seen that the peaks in LST were indexed to anatase, and only a weak peak at 27.3° ascribed to rutile was detected, implying that LST was composed of mostly anatase and a small amount of rutile, revealing that the inhibition of phase transformation by La doping was stronger than the promotion of Sn doping.

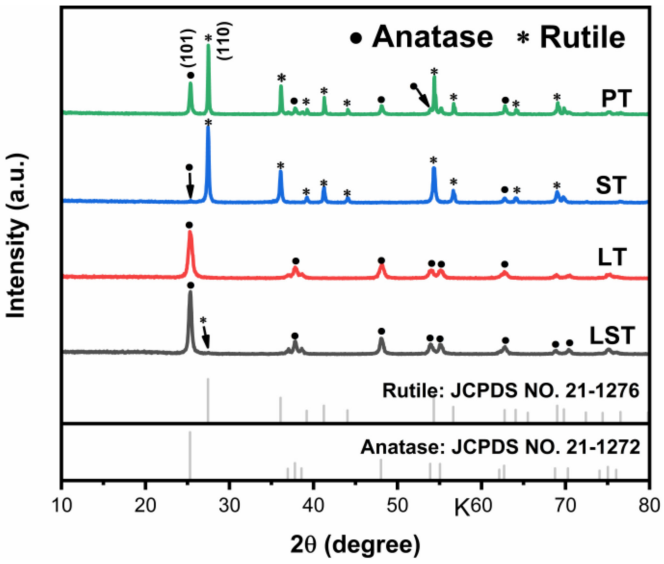

Figure 1. XRD patterns of samples.

Figure 2 presents the SEM images of samples. It can be observed that PT was composed of agglomerates with different shapes, and the size distribution of agglomerates ranged from tens to hundreds of nanometers. ST, LT, and LST samples were also composed of agglomerates of different shapes. No obvious change in particle morphology can be found in SEM images before and after doping.

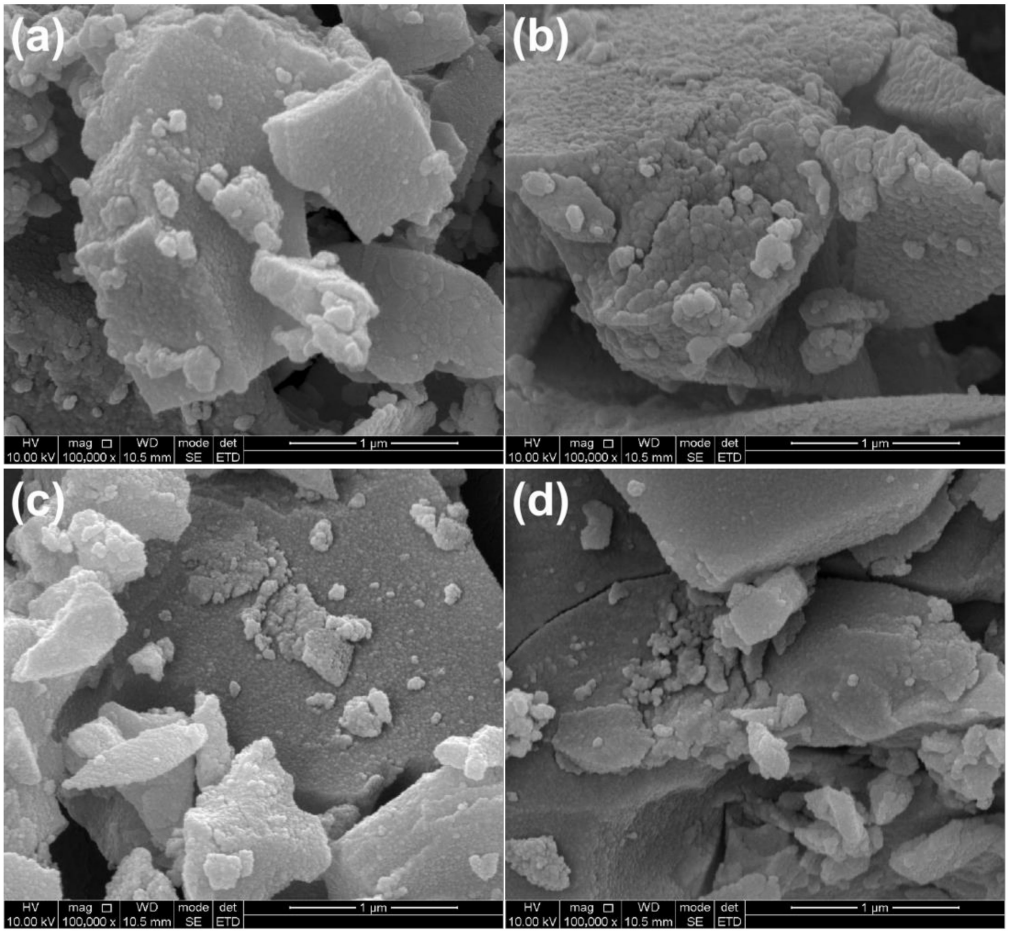

Figure 2. SEM images of PT (**a**), ST (**b**), LT (**c**), and LST (**d**).

Figure 3 shows the TEM images of PT (a) and LST (b). It can be observed that PT particles were seriously agglomerated, and it was difficult to distinguish the size of single particles. LST particles were also agglomerated, possibly due to the high temperature of 600 °C, and the particles grew larger during the process of heating. The HRTEM images of PT (c) and LST (d) are shown in Figure 3c,d. The crystal lattice stripes were clear, indicating that the samples had good crystallinity. The spacings of crystal planes marked in Figure 3c were 0.35 nm and 0.33 nm, corresponding to the anatase (101) crystal plane and the rutile (110) crystal plane, respectively [24–27], indicating that PT was a mixed crystal composed of anatase and rutile, consistent with the XRD results. The crystal plane spacing 0.36 nm marked in Figure 3d was indexed to the anatase (101) crystal plane of LST. The signals of Ti, O, La, and Sn elements could be found in the STEM mappings of LST (Figure 3e–k), indicating that La and Sn elements already existed in TiO_2 due to doping, and the four elements were substantially uniformly distributed in the LST sample.

Figure 4 presents the XPS spectra of PT and LST. The appearance of the La 3d peak and Sn 3d peak in the LST spectra confirms the existence of La and Sn elements in the co-doped sample. Figure 4b shows the high-resolution spectra of Ti 2p. The Ti 2p of PT was decomposed into two peaks, located at 458.5 eV and 464.1 eV, corresponding to Ti $2p_{3/2}$ and Ti $2p_{1/2}$, indicating that the valence state of Ti was +4. The two peaks corresponding to Ti $2p_{3/2}$ and Ti $2p_{1/2}$ were located at 458.6 eV and 464.3 eV in LST, indicating that Ti in the

co-doped sample also had a valence of +4 [15,28,29]. The high-resolution spectra of O 1s are shown in Figure 4c. The O 1s of PT was decomposed into two peaks corresponding to the lattice oxygen (O_L) and surface hydroxyl (O_H), located at 529.9 eV and 531.2 eV, respectively. The peaks of the lattice oxygen and surface hydroxyl of LST sample were at 530.0 eV and 531.1 eV respectively [30]. It can be observed that the surface hydroxyl peak area of the LST sample was significantly larger than that of PT, indicating that the co-doping advanced the surface adsorption performance and introduced more OH^- groups on the particle surface. The percentages of oxygen in the surface hydroxyl group of PT and LST were 12.1% and 22.6%, respectively, indicating that co-doping could enhance the surface hydroxyl content. This is beneficial to generate more hydroxyl radical and improve photocatalytic performance during photodegradation [31]. The Sn 3d high-resolution spectrum of LST is shown in Figure 4d. The two peaks at 486.3 eV and 494.9 eV corresponded to Sn $3d_{5/2}$ and Sn $3d_{3/2}$, respectively. The location of these two peaks indicates that the Sn element had a +4 valence [21,23,32]. The high-resolution spectrum of La 3d is shown in Figure 4e. The peaks at 834.8 eV and 838.1 eV corresponded to La $3d_{5/2}$, and the peaks at 852.2 eV and 855.1 eV corresponded to La $3d_{3/2}$, indicating that the La element existed in the form of La^{3+} [31,33].

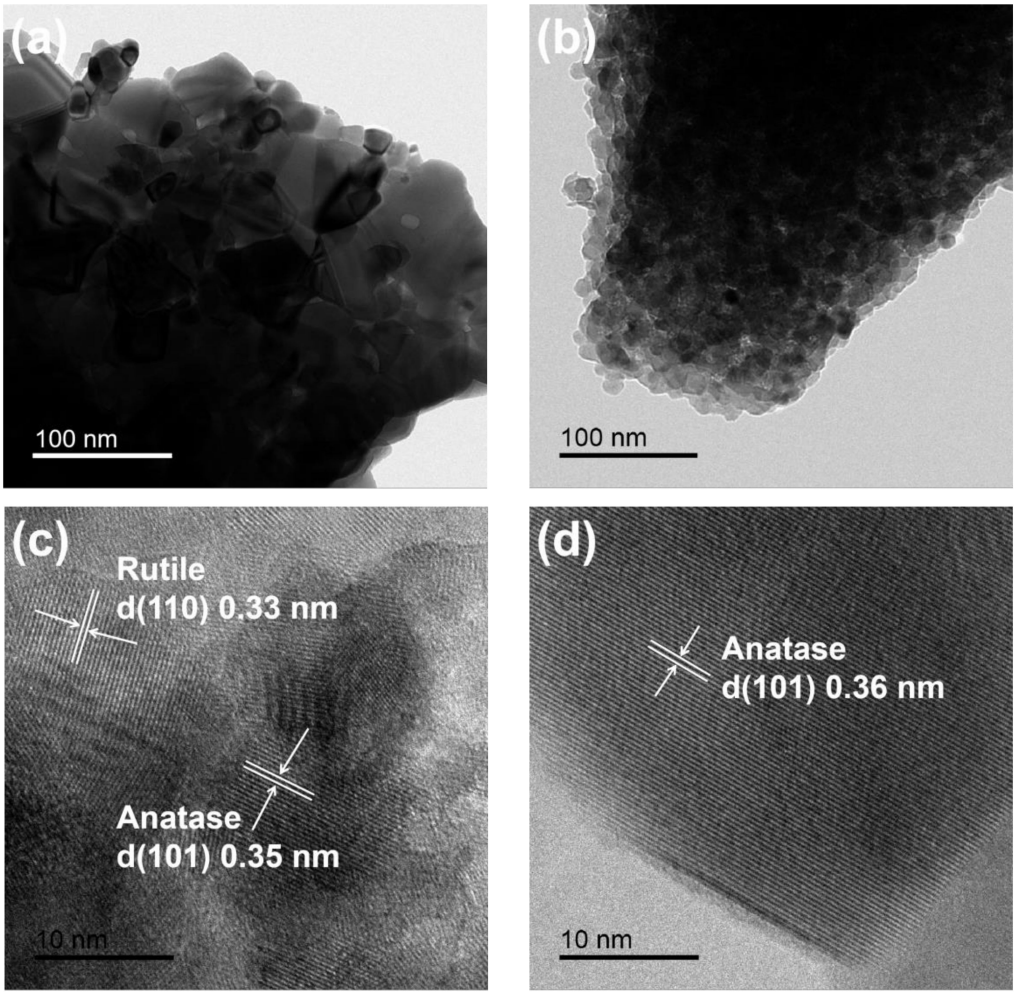

Figure 3. *Cont.*

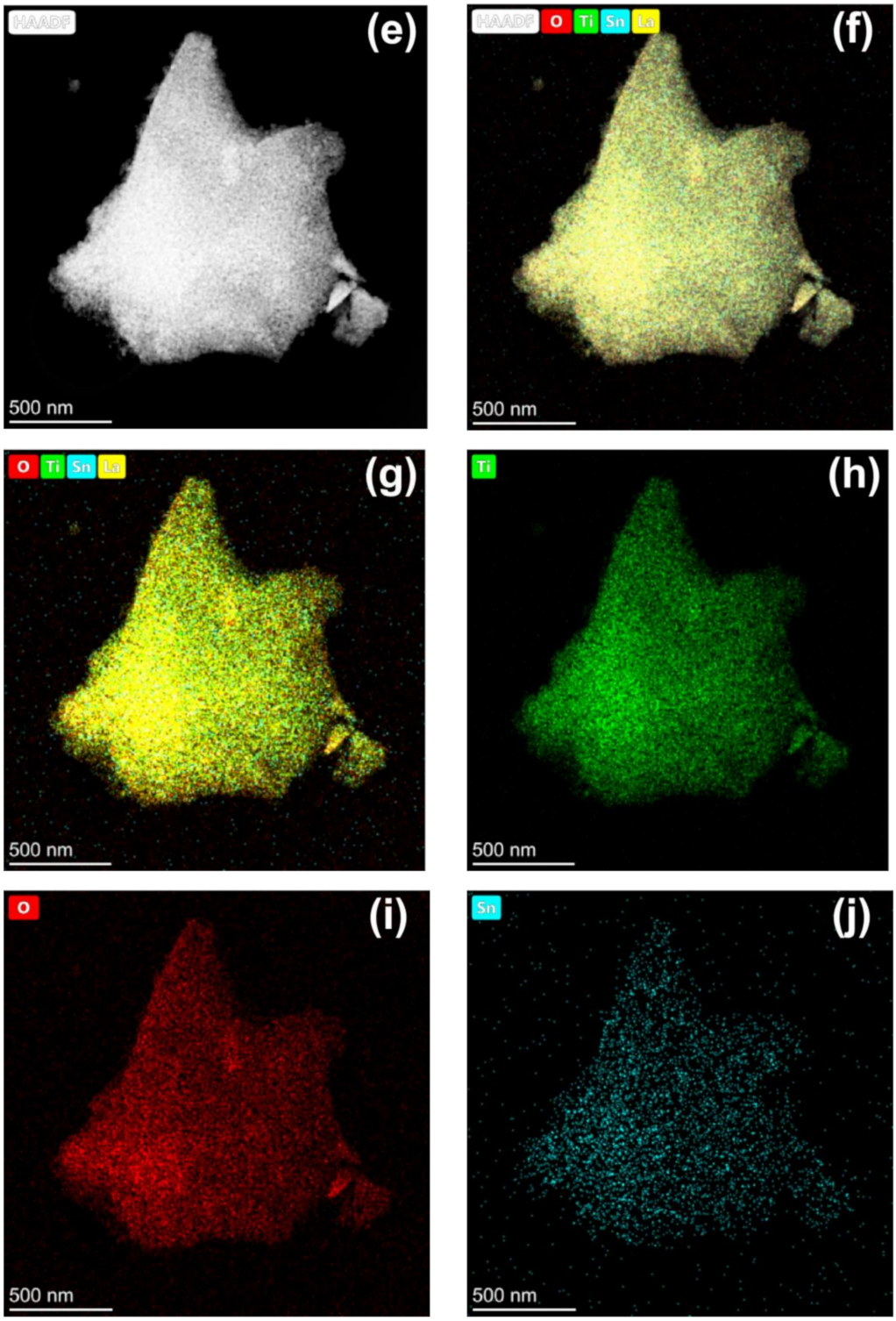

Figure 3. *Cont.*

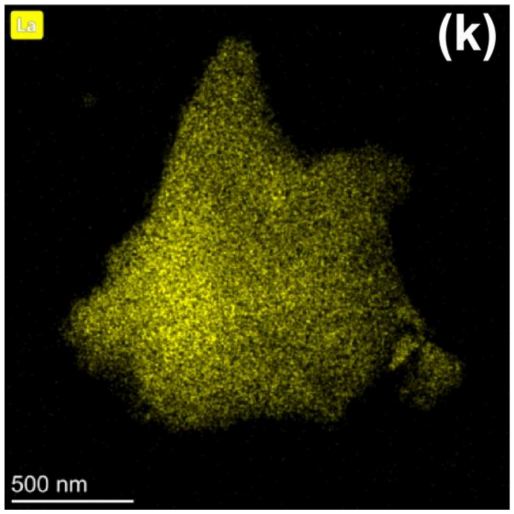

Figure 3. TEM and HRTEM images of PT (**a**,**c**) and LST (**b**,**d**), and the STEM mappings of LST (**e**–**k**).

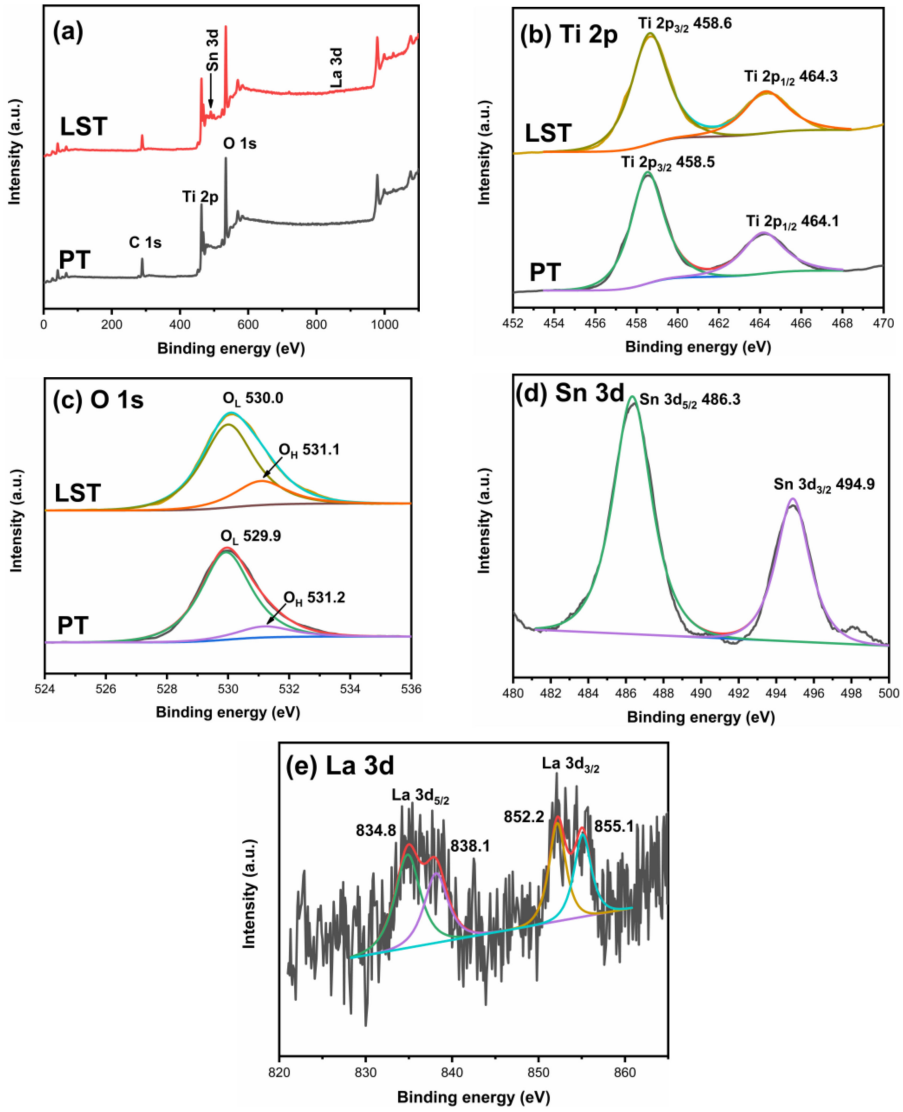

Figure 4. XPS survey of PT and LST (**a**); high resolution spectra of Ti 2p (**b**), O 1s (**c**), Sn 3d (**d**), and La 3d (**e**).

Figure 5 shows the UV/Vis absorption spectra (a) and the bandgap (b) of the samples. In the ultraviolet region, all samples had high absorption, whereas, in the visible region, absorption decreased rapidly. The absorption edge of ST was almost the same as that of PT, and the absorption edges of LT and LST showed a weak blue shift. The bandgaps of PT, ST, LT, and LST were 3.02, 3.02, 3.17, and 3.06 eV, respectively. It has been documented that the absorption edge of TiO_2 red-shifts and the bandgap decreases after Sn or La doping [31,34,35]. However, in this work, the bandgaps of LT and LST increased slightly. Combined with XRD, it can be seen that the transformation from anatase to rutile was inhibited by La doping. Due to the bandgap of anatase (3.2 eV) being larger than that of rutile (3.0 eV), the bandgaps of LT and LST samples increased compared to PT.

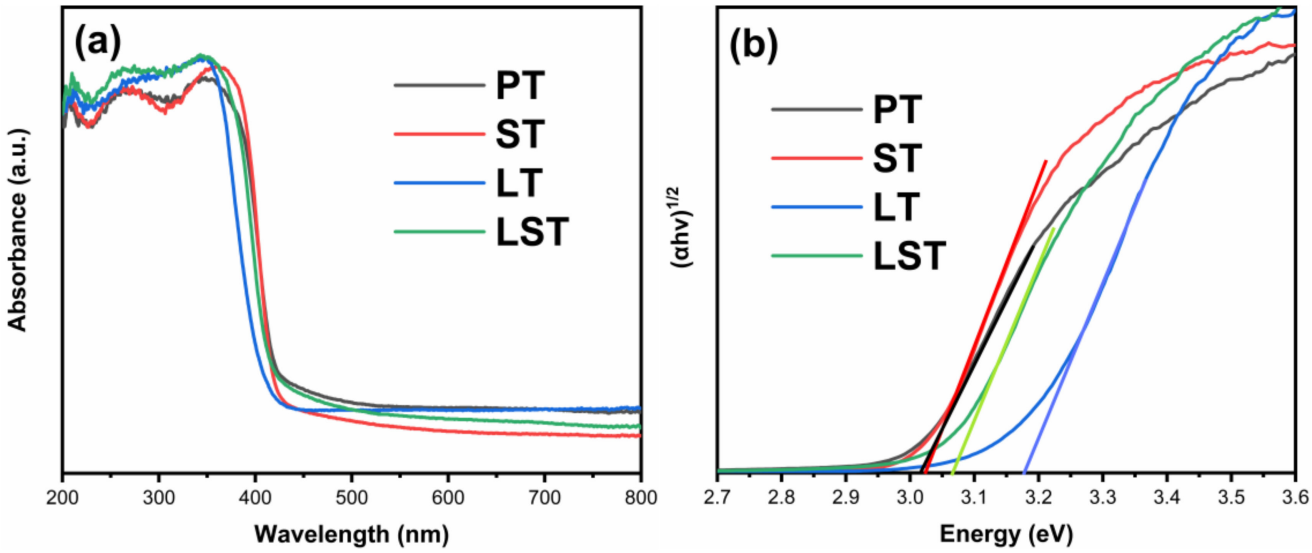

Figure 5. UV/Vis absorption spectra (**a**) and bandgap energy (**b**) of samples.

The PL spectra of samples are shown in Figure 6. PT and LST showed the same spectral shape but different intensity. The PL peak intensity decreased after Sn doping, indicating that the recombination of photogenerated electrons and holes was inhibited. The main PL peaks of PT and ST appeared at approximately 422 nm, due to the photons released when the photogenerated electrons returned directly from the conduction band to the valence band [32]. DRS results show that the bandgap of PT and ST was 3.02 eV, and the corresponding photon wavelength was 410 nm, which was about 12 nm less than the corresponding wavelength of 422 nm in the main peak of PL. This deviation could be attributed to the Stokes shift [36,37]. Compared with PT, the PL main peaks of LT and LST shifted to a lower wavelength, consistent with the bandgaps of LT and LST being larger than that of PT. The PL peak intensity of LT was lower than that of PT, indicating that La doping could also inhibit the recombination of photogenerated carriers. In particular, the PL peak intensity of LST was the lowest, implying that La/Sn co-doping had a synergistic effect on retarding the recombination of photogenerated charges, which was beneficial to the photocatalytic performance.

2.2. Photocatalytic Performance

Figure 7 shows the MB degradation degree curves (a) and kinetics curves (b) of samples. After 60 min, the degradation degree of PT was 59.3%, and the degradation degrees of ST, LT, and LST were 67.7%, 66.6%, and 80.6%, respectively. The degradation of MB on the surface of TiO_2 photocatalyst conformed to a first-order reaction, and the reaction rate constant k was calculated using the formula $kt = -\ln(C/C_0)$, where C_0 and C are the initial concentration of MB solution and the concentration at time t, respectively. A larger k value denotes a faster reaction rate and a better photocatalytic activity. The first-order reaction rate constants of PT, ST, LT, and LST were 0.015, 0.019, 0.018, and 0.027 min^{-1},

respectively. The first-order reaction rate constants of ST, LT, and LST are 1.3, 1.2, and 1.8 times higher than that of PT, respectively, indicating that the reaction rate was accelerated after doping. Table 1 summarizes the degradation degrees of reported photocatalysts.

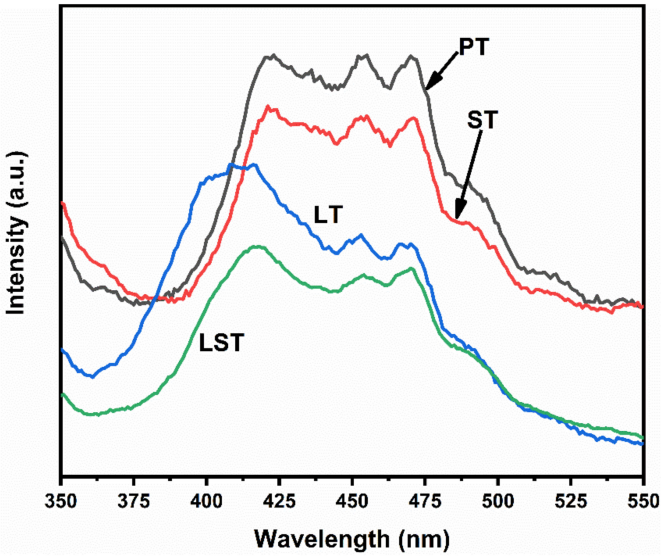

Figure 6. PL spectra of samples.

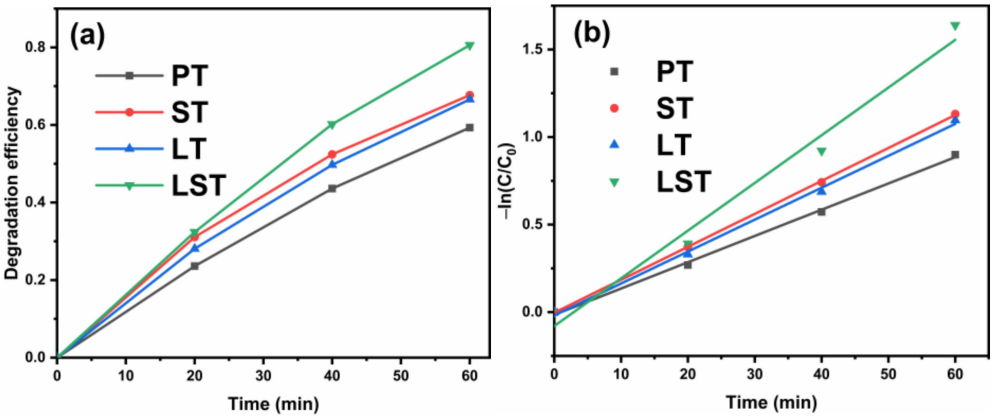

Figure 7. Degradation curves (100 mL of MB (10 mg/L) degraded by 0.05 g of sample at pH = 7 and room temperature of 25 °C) (**a**) and kinetics curves (**b**) of samples.

2.3. Photocatalytic Degradation Mechanism

Figure 8 shows the results active species experiments of LST. When benzoquinone (BQ), isopropanol (IPA), and ammonium oxalate (AO) were added as the radical scavengers, the degradation degrees of LST decreased from 80.6% to 28.1%, 61.5%, and 78.0%, respectively. Since BQ, IPA, and AO are capture agents of $\bullet O_2^-$, •OH, and photogenerated holes (h^+) [44,45], the results show that the $\bullet O_2^-$ radical was the main active group, whereas h^+ and •OH played a subsidiary role in the degradation process toward MB.

Nitro-blue tetrazolium (NBT) and 2,3-dihydroxybenzoic acid (2,3-HBA) experiments were launched to further verify that the $\bullet O_2^-$ and •OH radicals were yielded in the degradation process, and the results are shown in Figure 9. The presence of $\bullet O_2^-$ radicals can be testified by the reaction of NBT with $\bullet O_2^-$ to form a purple precipitate. With the extension of illumination time, the $\bullet O_2^-$ radicals react with NBT to generate more and more purple precipitates, thus consuming NBT and gradually reducing its absorbance. On the other hand, salicylic acid (SA) reacts with •OH radicals to form 2,3-HBA which has a special absorption at 510 nm [44,45]. With the increase in time, the absorbance of NBT

decreased and the absorbance of 2,3-HBA increased, indicating that $\bullet O_2^-$ radicals and •OH radicals were generated in the system.

Table 1. The summarization of degradation degrees by various photocatalysts.

Ref.	Method	Photocatalyst	Light Source	Target Pollutant	Decolorization Degree
[29]	Sol–gel method	Fe–TiO_2	UV light (15 W)	RB 69 (100 mg/L)	98.0% in 120 min
[31]	Sol–gel method	La–N–TiO_2/diatomite	Xenon lamp (150 W)	RhB (10 mg/L)	93.0% in 240 min
[38]	Combustion synthesis methodology	Mg_2Si(Si)/MgO	LED lamp (100 W)	MB (50 mg/L)	90.0% in 120 min
[39]	Ball-milling/molten salt processing approach	Co_3Fe_7/$CoFe_2O_4$@ carbon	LED lamp (100 W)	MB (100 mg/L)	100% in 12 min
[40]	Acid-treatment method	Mg_2Si	LED lamp (100 W)	MO (50 ppm)	100% in 30 min
[41]	Hydrothermal method	SDBS–TiO_2	Xenon lamp (500 W)	RhB (10 mg/L)	90.0% in 120 min
[42]	Hydrothermal method	Ag–TiO_2	Xenon lamp (500 W)	RhB (20 mg/L)	80.0% in 240 min
[43]	Electrospinning method	Fe–ZnO	Mercury lamp	MB (10 mg/L)	88.0% in 360 min
[44]	Solvothermal method	BiOI/Bi_2SiO_5	Xenon lamp (500 W)	MO (10 ppm)	70.0% in 360 min
This work	Sol–gel method	La–Sn–TiO_2	Xenon lamp (250 W)	MB (10 mg/L)	80.6% in 60 min

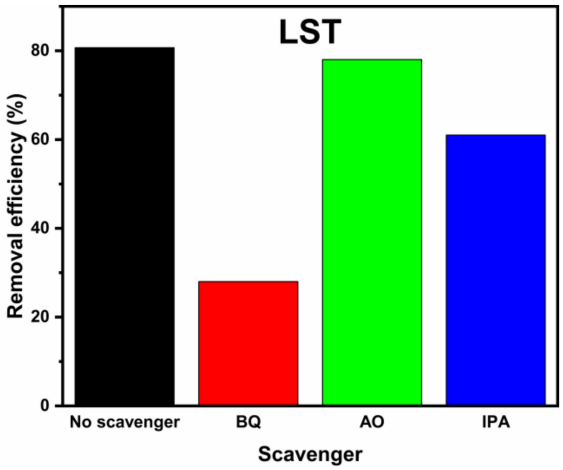

Figure 8. Degradation degrees of LST in the presence of different scavengers.

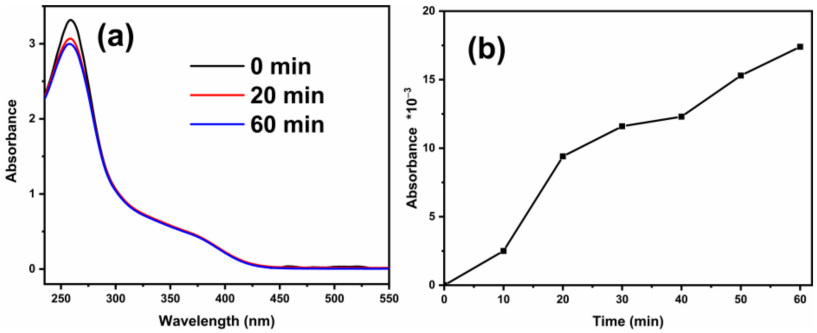

Figure 9. Absorbance curves of NBT (**a**) and 2,3-HBA (**b**) of LST.

Figure 10 shows the NBT and 2,3-HBA absorbance of LST and PT after illumination for 20 min. The NBT absorbance of PT was higher than that of LST, indicating that LST generated more $\bullet O_2^-$ radicals. The 2,3-HBA absorbance of PT was lower than that of LST, proving that LST produced more •OH radicals. During the photodegradation process, LST generated more free radicals, implying that it had a higher photogenerated charge separation rate compared to PT, consistent with the results of the PL spectra and photocatalytic activity experiments.

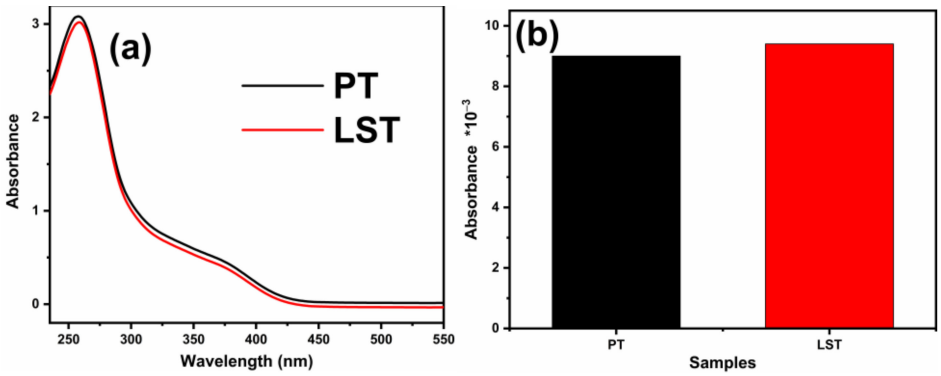

Figure 10. NBT absorbance (**a**) and 2,3-HBA (**b**) absorbance of LST and PT after 20 min.

The separation and transfer of photogenerated charges of PT and LST were further studied through photoelectrochemical measurements. Figure 11a shows the photocurrent responses curves (PC) of PT and LST. Generally, a higher photocurrent density denotes a higher separation efficiency of photogenerated charges [46,47]. Both PT and LST generated photocurrent under light, and the photocurrent density of LST was higher than that of PT, indicating that Sn and La co-doping was beneficial to improve the separation efficiency of carriers. Figure 11b shows the electrochemical impedance spectra (EIS) of PT and LST. According to Nyquist's theorem [46,48,49], the arc radius of LST was smaller than that of PT, indicating that LST had a lower charge motion resistance and a better electron mobility.

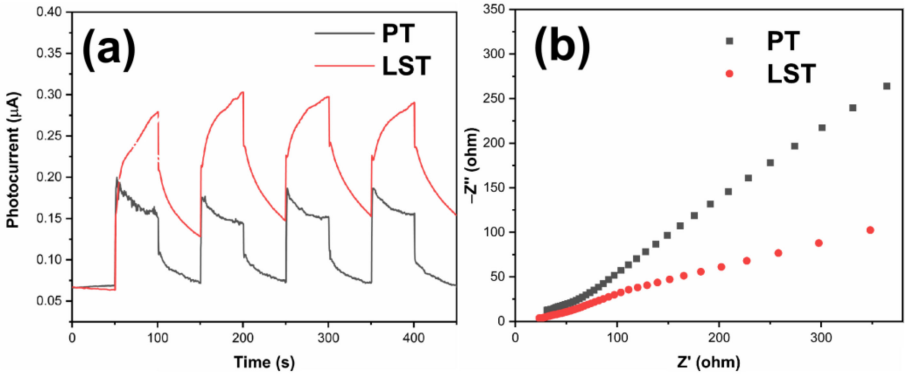

Figure 11. Photocurrent responses curves (**a**) and electrochemical impedance spectroscopy (**b**) of PT and LST.

Figure 12 shows the Schottky curves of PT and LST. The electrode/electrolyte was is measured according to the Mott–Schottky equation (1) [48,50,51].

$$\frac{1}{C^2} = \frac{2}{N_D e \varepsilon_0 \varepsilon}\left(E - E_{FB} - \frac{kT}{e}\right), \quad (1)$$

where C is the space charge capacitance in the semiconductor, N_D is the electron carrier density, e is the elemental charge, ε_0 is the permittivity of a vacuum, ε is the relative permittivity of the semiconductor, E is the applied potential, E_{FB} is the flat band potential,

T is the temperature, and k is the Boltzmann constant. The slope of the linear part of the curve was positive, indicating that LST is an n-type semiconductor [48,49,51]. In Equation (1), if $1/C^2 = 0$, the E_{FB} value of the LST flat band potential could be estimated to be −0.55 V vs. Ag/AgCl. According to the formula $E_{NHE} = E_{Ag/AgCl} + 0.197$ [52–54], the E_{FB} of LST could be calculated to be about −0.35 V vs. NHE. It is generally believed that the CB bottom (E_{CB}) is about 0.1 V more negative than the potential of E_{FB} for n-type semiconductors [55,56]. Therefore, the E_{CB} of LST could be determined to be −0.45 V vs. NHE. According to the formula $E_{VB} = E_g + E_{CB}$ [49,51], the potential of VB (E_{VB}) of LST could be calculated to be +2.61 V vs. NHE.

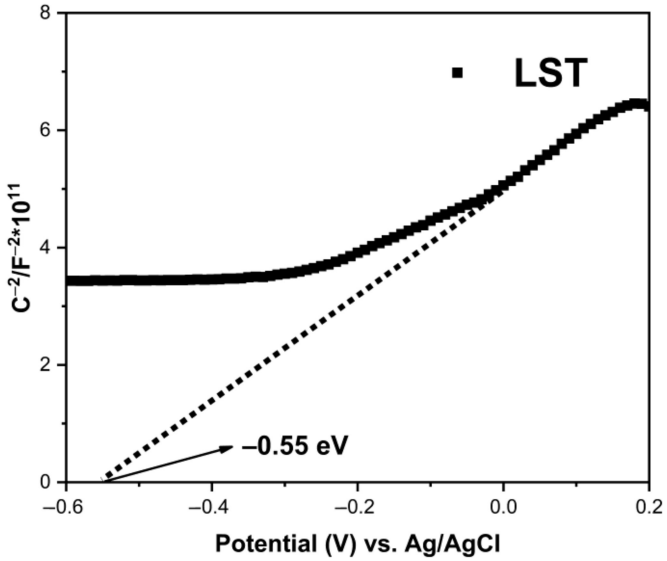

Figure 12. Mott–Schottky plot of LST.

Some studies reported that ion doping brings impurity energy levels below the conduction band of TiO_2, reduces the bandgap width, and increases the absorption of light [20,23]. Conversely, several studies also showed that there is a blue shift after doping [57,58]. In this work, DRS results show that the bandgap width of PT was 3.02 eV and that of LST was 3.06 eV, without a red shift, which could be ascribed to the fact that co-doping of Sn and La inhibited the transformation from anatase to rutile, and the forbidden band width of rutile was lower than that of anatase. Consequently, a weak blue shift occurred after La/Sn co-doping, implying that the utilization of visible light did not improve via co-doping. It can be seen from PL spectra that single doping of Sn and La or co-doping could inhibit the recombination of photogenerated electrons and holes, and LST exhibited the best inhibition ability. According to the DRS and Mott–Schottky results, the E_{CB} of LST was −0.45 V, which is higher than $E_0(O_2/\bullet O_2^-)$ (−0.046 V vs. NHE) [59,60]. The potential position of CB ensured the generation of $\bullet O_2^-$ radicals, as also confirmed by NBT experiments. On the basis of the above results, the mechanism diagram of photodegradation of MB by LST is shown in Figure 13.

On one hand, as the radius of Sn^{4+} is close to that of Ti^{4+}, the replacement of Ti^{4+} by Sn^{4+} ions would form crystal defects, capture photogenerated charges, and improve quantum efficiency [61–63]. On the other hand, no peak related to La element was detected in the XRD pattern. The radius of La^{3+} ions is much larger than that of Ti^{4+} ions; thus, the possibility that La^{3+} ions entered the TiO_2 lattice can be excluded. Instead they were dispersed on the surface of TiO_2 particles in the form of oxide La_2O_3, which captured photogenerated charges, improving the separation of carriers [16,33,64]. Therefore, the co-doping of Sn and La produced a synergistic effect on improving the carrier separation; as a result, its photocatalytic activity was higher than that of single-element doping in PT.

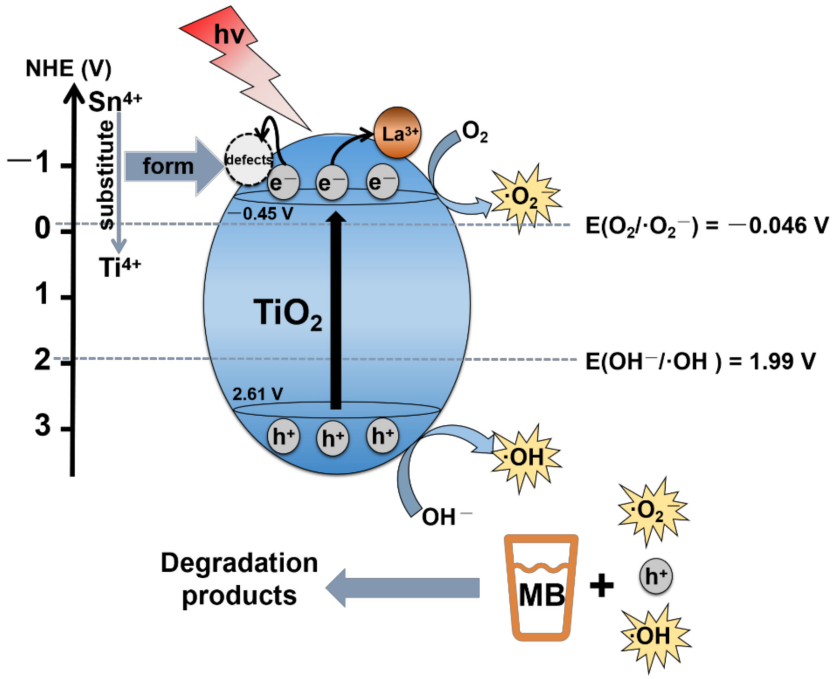

Figure 13. Schematic diagram of MB photodegradation by LST.

3. Materials and Methods

Butyl titanate (Analytical Reagent, AR, ≥98.0%), anhydrous ethanol (AR, ≥99.7%), glacial acetic acid (AR, ≥99.5%), tin tetrachloride pentahydrate (AR, ≥99.0%), lanthanum nitrate hexahydrate (AR, ≥99.0%), benzoquinone (AR, ≥98.5%), ammonium oxalate (AR, ≥99.5%), and isopropanol (AR, ≥99.7%) were purchased from Chengdu Chron Chemicals Co., Ltd., (Chengdu, China).

3.1. Sample Preparation

Butyl titanate and anhydrous ethanol were added into the beaker at a volume ratio of 1:2 to form solution A. Deionized water, glacial acetic acid and anhydrous ethanol were mixed in a volume ratio of 2:3:7.5 to form solution B. After being evenly stirred, solution B was dropped into solution A, which was continuously stirred to form sol and then aged. After the aging, the gel was dried in the oven, and finally heat-treated at 600 °C. After grinding, pure TiO_2 powder was obtained, labeled as PT. Certain amounts of $SnCl_4 \cdot 5H_2O$ and $La(NO_3)_3 \cdot 6H_2O$ were added to solution B, and the other steps were the same to prepare the doped sample with a Sn/Ti molar ratio of 3% and a La/Ti molar ratio of 0.5%. Sn/La co-doped TiO_2 could be prepared by adding $SnCl_4 \cdot 5H_2O$ and $La(NO_3)_3 \cdot 6H_2O$ into solution B, where the molar ratio of Sn/Ti was 3% and the molar ratio of La/Ti was 0.5%. Sn-doped TiO_2, La-doped TiO_2, and La/Sn co-doped TiO_2 were labeled as ST, LT, and LST, respectively.

3.2. Sample Characterization

The crystal structure of the samples was analyzed using a DX-2700 X-ray diffractometer (Dandong Haoyuan Instrument Co. Ltd., Dandong, China, XRD). An FEI-Inspect F50 scanning electron microscope (FEI Company, Hillsboro, OR, USA, SEM) and an FEI-Tecnai G2 F20 transmission electron microscope (FEI Company, Hillsboro, OR, USA, TEM and HRTEM) were used to observe the morphology. An XSAM800 multifunctional surface analysis system was used to analyze the element composition and valence state of samples (Kratos Ltd., Manchester, UK, XPS). A UV-3600 ultraviolet/visible-light spectrophotometer was used to study the optical absorption performance (Shimadzu Group Company, Kyoto, Japan, DRS). Detection of the recombination of photogenerated electrons and holes was investigated using an F-4600 fluorescence spectrometer (Shimadzu Group Company, Kyoto,

Japan, PL). The photocurrent response curves, electrochemical impedance spectroscopy, and Mott–Schottky plots were measured using a DH-7000 electrochemical workstation (Jiangsu Donghua Analytical Instrument Co., Ltd., China, PC, EIS and MS).

3.3. Photocatalysis Experiment

The photocatalytic activity of the sample was evaluated with MB solution as the target pollutant. Briefly, 100 mL of MB (10 mg/L) solution and 0.05 g of sample powder were mixed at room temperature (25 °C) and kept neutral. After stirring for 30 min in the dark, the mixture was irradiated using a 250 W xenon lamp (300–800 nm). Samples were taken every 20 min. The absorbance of the supernatant was tested at 664 nm. The MB degradation degree was calculated using the formula $(A_0 - A_t)/A_0 \times 100\%$, where A_0 and A_t are the initial and time t absorbances of MB.

On the basis of the MB degradation system, 2 mL (0.1 mol/L) of benzoquinone (BQ, $\bullet O_2^-$ trapping agent), isopropanol (IPA, •OH trapping agent), and ammonium oxalate (AO, h^+ trapping agent) were added to investigate the active species.

4. Conclusions

Pure TiO_2 was prepared using the sol–gel method and modified by La/Sn single doping and co-doping. PT had an anatase/rutile mixed crystalline structure, Sn promoted the transformation from anatase to rutile, and La inhibited the transformation. The inhibition of La was stronger than that of Sn, and the phase transformation from anatase to rutile was inhibited by co-doping. La/Sn co-doping did not produce an obvious red shift; however, the content of hydroxyl on the surface of TiO_2 particles increased, and a synergistic effect was produced on inhibiting the recombination of photogenerated electrons and holes. The results of electrochemical experiments also showed that the separation and transfer of photogenerated charges were faster after La/Sn co-doping, and the quantum efficiency was improved. Therefore, the photocatalytic activity of LST was superior to that of ST, LT, and PT. The first-order reaction rate constant of PT was 0.015 min^{-1}, and the first-order reaction rate constants of ST, LT, and LST were 1.3, 1.2, and 1.8 times higher than that of PT, respectively. The active species experiments of LST showed that $\bullet O_2^-$ radicals were the main active groups during the photodegradation process.

Author Contributions: Methodology, X.Z., Y.J. and W.F.; investigation, F.Q. and L.H.; writing—original draft preparation, F.Q.; writing—review and editing, L.H.; supervision, W.F.; project administration, X.Z.; formal analysis, Y.J. and X.Z.; funding acquisition, X.Z. All authors have read and agreed to the published version of the manuscript.

Funding: This study was supported by the Key Research and Development Projects of Liangshan Prefecture Science and Technology Bureau of Sichuan Province (21ZDYF0202), the Higher-Education Talent Quality and Teaching Reform Project of Sichuan Province (JG2021-1104), and the Talent Training Quality and Teaching Reform Project of Chengdu University (cdjgb2022033).

Institutional Review Board Statement: Not applicable.

Informed Consent Statement: Not applicable.

Data Availability Statement: Not applicable.

Conflicts of Interest: The authors declare no conflict of interest.

References

1. Sun, Y.; Liu, E.D.; Zhu, L.; Wen, Y.; Tan, Q.W.; Feng, W. Influence of annealing temperature of TiO_2 nanotubes via hydrothermal method on Ti foil for photocatalytic degradation. *Dig. J. Nanomater. Bios.* **2019**, *14*, 463–470.
2. Zhu, X.D.; Xu, H.Y.; Yao, Y.; Liu, H.; Wang, J.; Pu, Y.; Feng, W.; Chen, S.H. Effects of Ag^0-modification and Fe^{3+}-doping on the structural, optical and photocatalytic properties of TiO_2. *RSC Adv.* **2019**, *9*, 40003–40012. [CrossRef] [PubMed]
3. Sun, Y.; Xu, S.; Zeng, J.Y.; Yang, S.S.; Zhao, Q.R.; Yang, Y.; Zhao, Q.; Wang, G.X. Fabrication and photocatalytic activity of TiO_2 nanotubes by hydrothermal treatment. *Dig. J. Nanomater. Bios.* **2021**, *16*, 239–246.

4. Wu, D.; Li, C.; Zhang, D.S.; Wang, L.L.; Zhang, X.P.; Shi, Z.F.; Lin, Q. Photocatalytic improvement of Y^{3+} modified TiO_2 prepared by a ball milling method and application in shrimp wastewater treatment. *RSC Adv.* **2019**, *9*, 14609–14620. [CrossRef]
5. Solís-Casados, D.A.; Escobar-Alarcón, L.; Gómez-Oliván, L.M.; Haro-Poniatowski, E.; Klimova, T. Photodegradation of pharmaceutical drugs using Sn-modified TiO_2 powders under visible light irradiation. *Fuel* **2017**, *198*, 3–10. [CrossRef]
6. Yan, J.K.; Rong, X.Q.; Gu, X.; Du, J.H.; Gan, G.Y. Phase composition and photocatalytic properties of La^{3+}-doped TiO_2 nanopowders. *Rare Metal Mat. Eng.* **2020**, *49*, 0465–0475.
7. Umar, K.; Ibrahim, M.N.M.; Ahmad, A.; Rafatullah, M. Synthesis of Mn-doped TiO_2 by novel route and photocatalytic mineralization/intermediate studies of organic pollutants. *Res. Chem. Intermediat.* **2019**, *45*, 2927–2945. [CrossRef]
8. Zhang, W.; Li, X.J.; Jia, G.; Gao, Y.F.; Wang, H.; Cao, Z.Z.; Li, C.H.; Liu, J.R. Preparation, characterization, and photocatalytic activity of boron and lanthanum co-doped TiO_2. *Catal. Commun.* **2014**, *45*, 144–147. [CrossRef]
9. Huang, T.Z.; Mao, S.; Yu, J.M.; Wen, Z.H.; Lu, G.H.; Chen, J.H. Effects of N and F doping on structure and photocatalytic properties of anatase TiO_2 nanoparticles. *RSC Adv.* **2013**, *3*, 16657–16664. [CrossRef]
10. Lin, X.X.; Rong, F.; Fu, D.G.; Yuan, C.W. Enhanced photocatalytic activity of fluorine doped TiO_2 by loaded with Ag for degradation of organic pollutants. *Powder Technol.* **2012**, *219*, 173–178. [CrossRef]
11. Wang, Y.Z.; Wu, Y.S.; Yang, H.; Xue, X.X.; Liu, Z.H. Doping TiO_2 with boron or/and cerium elements: Effects on photocatalytic antimicrobial activity. *Vacuum* **2016**, *131*, 58–64. [CrossRef]
12. Adyani, S.M.; Ghorbani, M. A comparative study of physicochemical and photocatalytic properties of visible light responsive Fe, Gd and P single and tri-doped TiO_2 nanomaterials. *J. Rare Earths* **2018**, *36*, 72–85. [CrossRef]
13. Kalantari, K.; Kalbasi, M.; Sohrabi, M.; Royaee, S.J. Enhancing the photocatalytic oxidation of dibenzothiophene using visible light responsive Fe and N co-doped TiO_2 nanoparticles. *Ceram. Int.* **2017**, *43*, 973–981. [CrossRef]
14. Shaban, M.; Ahmed, A.M.; Shehata, N.; Betiha, M.A.; Rabie, A.M. Ni-doped and Ni/Cr co-doped TiO_2 nanotubes for enhancement of photocatalytic degradation of methylene blue. *J. Colloid Interface Sci.* **2019**, *555*, 31–41. [CrossRef]
15. Chen, Y.; Liu, K.R. Fabrication of Ce/N co-doped TiO_2/diatomite granule catalyst and its improved visible-light-driven photoactivity. *J. Hazard. Mater.* **2017**, *324*, 139–150. [CrossRef]
16. Nešić, J.; Manojlović, D.D.; Andelković, I.; Dojcinović, B.P.; Vulić, P.J.; Krstić, J.; Roglić, G.M. Preparation, characterization and photocatalytic activity of lanthanum and vanadium co-doped mesoporous TiO_2 for azo-dye degradation. *J. Mol. Catal. A Chem.* **2013**, *378*, 67–75. [CrossRef]
17. Peng, H.; Cui, J.; Zhan, H.J.; Zhang, X. Improved photodegradation and detoxification of 2,4,6-trichlorophenol by lanthanum doped magnetic TiO_2. *Chem. Eng. J.* **2015**, *264*, 316–321. [CrossRef]
18. Xin, Y.J.; Liu, H.L. Study on mechanism of photocatalytic performance of La-doped TiO_2/Ti photoelectrodes by theoretical and experimental methods. *J. Solid State Chem.* **2011**, *184*, 3240–3246. [CrossRef]
19. Cruz, D.D.L.; Arévalo, J.C.; Torres, G.; Margulis, B.R.G.; Ornelas, C.; Aguilar-Elguézabal, A. TiO_2 doped with Sm^{3+} by sol-gel: Synthesis, characterization and photocatalytic activity of diuron under solar light. *Catal. Today* **2011**, *166*, 152–158. [CrossRef]
20. Mohamed, R.M.; Aazam, E.S. Effect of Sn loading on the photocatalytic aniline synthesis activity of TiO_2 nanospheres. *J. Alloys Compd.* **2014**, *595*, 8–13. [CrossRef]
21. Li, J.L.; Xu, X.T.; Liu, X.J.; Yu, C.Y.; Yan, D.; Sun, Z.; Pan, L.K. Sn doped TiO_2 nanotube with oxygen vacancy for highly efficient visible light photocatalysis. *J. Alloys Compd.* **2016**, *679*, 454–462. [CrossRef]
22. Alves, A.K.; Berutti, F.A.; Bergmann, C.P. Visible and UV photocatalytic characterization of Sn-TiO_2 electrospun fibers. *Catal. Today* **2013**, *208*, 7–10. [CrossRef]
23. Li, J.; Shi, J.; Li, Y.B.; Ding, Z.L.; Huang, J.G. A biotemplate synthesized hierarchical Sn-doped TiO_2 with superior photocatalytic capacity under simulated solar light. *Ceram. Int.* **2021**, *47*, 8218–8227. [CrossRef]
24. Dong, P.M.; Cheng, X.D.; Huang, Z.F.; Chen, Y.; Zhang, Y.Z.; Nie, X.X.; Zhang, X.W. In-situ and phase controllable synthesis of nanocrystalline TiO_2 on flexible cellulose fabrics via a simple hydrothermal method. *Mater. Res. Bull.* **2018**, *97*, 89–95. [CrossRef]
25. Nguyen-Phan, T.D.; Pham, V.H.; Chung, J.S.; Chhowalla, M.; Asefa, T.; Kim, W.J.; Shin, E.W. Photocatalytic performance of Sn-doped TiO_2/reduced graphene oxide composite materials. *Appl. Catal. A Gen.* **2014**, *473*, 21–30. [CrossRef]
26. Wu, M.C.; Wu, P.Y.; Lin, T.H.; Lin, T.F. Photocatalytic performance of Cu-doped TiO_2 nanofibers treated by the hydrothermal synthesis and air-thermal treatment. *Appl. Surf. Sci.* **2018**, *430*, 390–398. [CrossRef]
27. Tang, M.; Xia, Y.W.; Yang, D.X.; Lu, S.J.; Zhu, X.D.; Tang, R.Y.; Zhang, W.M. Ag decoration and SnO_2 coupling modified anatase/rutile mixed crystal TiO_2 composite photocatalyst for enhancement of photocatalytic degradation towards tetracycline hydrochloride. *Nanomaterials* **2022**, *12*, 873. [CrossRef]
28. Zhu, X.D.; Wen, G.L.; Liu, H.; Han, S.H.; Chen, S.H.; Kong, Q.Q.; Feng, W. One-step hydrothermal synthesis and characterization of Cu-doped TiO_2 nanoparticles/nanobucks/nanorods with enhanced photocatalytic performance under simulated solar light. *J. Mater. Sci. Mater Electron.* **2019**, *30*, 13826–13834. [CrossRef]
29. Mathews, N.R.; Cortes Jacome, M.A.; Angeles-Chavez, C.; Toledo Antonio, J.A. Fe doped TiO_2 powder synthesized by sol gel method: Structural and photocatalytic characterization. *J. Mater. Sci. Mater. Electron.* **2015**, *26*, 5574–5584. [CrossRef]
30. Zhu, X.D.; Zhou, Q.; Xia, Y.W.; Wang, J.; Chen, H.J.; Xu, Q.; Liu, J.W.; Feng, W.; Chen, S.H. Preparation and characterization of Cu-doped TiO_2 nanomaterials with anatase/rutile/brookite triphasic structure and their photocatalytic activity. *J. Mater. Sci. Mater. Electron.* **2021**, *32*, 21511–21524. [CrossRef]

31. Chen, Y.; Wu, Q.; Zhou, C.; Jin, Q.T. Enhanced photocatalytic activity of La and N co-doped TiO_2/diatomite composite. *Powder Technol.* **2017**, *322*, 296–300. [CrossRef]
32. Zhu, X.D.; Zhu, R.R.; Pei, L.X.; Liu, H.; Xu, L.; Wang, J.; Feng, W.; Jiao, Y.; Zhang, W.M. Fabrication, characterization, and photocatalytic activity of anatase/rutile/SnO_2 nanocomposites. *J. Mater. Sci. Mater. Electron.* **2019**, *30*, 21210–21218. [CrossRef]
33. Yu, Y.M.; Piao, L.J.; Xia, J.X.; Wang, W.Z.; Geng, J.F.; Chen, H.Y.; Xing, X.; Li, H. A facile one-pot synthesis of N-La codoped TiO_2 porous materials with bio-hierarchical architectures and enhanced photocatalytic activity. *Mater. Chem. Phys.* **2016**, *182*, 77–85. [CrossRef]
34. Jiang, H.Q.; Liu, Y.D.; Li, J.S.; Wang, H.Y. Synergetic effects of lanthanum, nitrogen and phosphorus tri-doping on visible-light photoactivity of TiO_2 fabricated by microwave-hydrothermal process. *J. Rare Earth* **2016**, *34*, 604–613. [CrossRef]
35. Tripathi, A.K.; Mathpal, M.C.; Kumar, P.; Singh, M.K.; Soler, M.A.G.; Agarwal, A. Structural, optical and photoconductivity of Sn and Mn doped TiO_2 nanoparticles. *J. Alloys Compd.* **2015**, *622*, 37–47. [CrossRef]
36. Wang, S.X.; Song, Z.; Kong, Y.W.; Liu, Q.L. Relationship of Stokes shift with composition and structure in Ce^{3+}/Eu^{2+}-doped inorganic compounds. *J. Lumin.* **2019**, *212*, 250–263. [CrossRef]
37. Khaidukov, N.M.; Makhov, V.N.; Zhang, Q.H.; Shi, R.; Liang, H.B. Extended broadband luminescence of dodecahedral multisite Ce^{3+} ions in garnets $\{Y_3\}[MgA](BAlSi)O_{12}$ (A = Sc, Ga, Al; B = Ga, Al). *Dyes Pigments* **2017**, *142*, 524–529. [CrossRef]
38. Kamali, A.R.; Zhu, W.H.; Shi, Z.N.; Wang, D.X. Combustion synthesis-aqueous hybridization of nanostructured graphene-coated silicon and its dye removal performance. *Mater. Chem. Phys.* **2022**, *277*, 125565. [CrossRef]
39. Wei, S.H.; Kamali, A.R. Waste plastic derived Co_3Fe_7/$CoFe_2O_4$@carbon magnetic nanostructures for efficient dye adsorption. *J. Alloys Compd.* **2021**, *886*, 161201. [CrossRef]
40. Zhao, Z.Y.; Kamali, A.R. One-step conversion of Mg_2Si into hydrogen-terminated porous silicon nanostructures. *Mater. Today Chem.* **2021**, *22*, 100621. [CrossRef]
41. Si, Y.J.; Liu, H.H.; Li, N.T.; Zhong, J.B.; Li, J.Z.; Ma, D.M. SDBS-assisted hydrothermal treatment of TiO_2 with improved photocatalytic activity. *Mater. Lett.* **2018**, *212*, 147–150. [CrossRef]
42. Huang, J.; Ding, L.; Xi, Y.N.; Shi, L.; Su, G.; Gao, R.J.; Wang, W.; Dong, B.H.; Cao, L.X. Efficient silver modification of TiO_2 nanotubes with enhanced photocatalytic activity. *Solid State Sci.* **2018**, *80*, 116–122. [CrossRef]
43. Liu, L.; Liu, Z.W.; Yang, Y.X.; Geng, M.Q.; Zou, Y.M.; Shahzad, M.B.; Dai, Y.X.; Qi, Y. Photocatalytic properties of Fe-doped ZnO electrospun nanofibers. *Ceram. Int.* **2018**, *44*, 19998–20005. [CrossRef]
44. Dou, L.; Zhong, J.B.; Li, J.Z.; Pandian, R.; Burda, C. In-situ construction of 3D nanoflower-like BiOI/Bi_2SiO_5 heterojunctions with enhanced photocatalytic performance for removal of decontaminants originated from a step-scheme mechanism. *Appl. Surf. Sci.* **2021**, *544*, 148883. [CrossRef]
45. Zhu, X.D.; Wang, J.; Yang, D.X.; Liu, J.W.; He, L.L.; Tang, M.; Feng, W.; Wu, X.Q. Fabrication, characterization and high photocatalytic activity of Ag-ZnO heterojunctions under UV-visible light. *RSC Adv.* **2021**, *11*, 27257–27266. [CrossRef]
46. Dou, L.; Jin, X.Y.; Chen, J.F.; Zhong, J.B.; Li, J.Z.; Zeng, Y.; Duan, R. One-pot solvothermal fabrication of S-scheme OVs-Bi_2O_3/Bi_2SiO_5 microsphere heterojunctions with enhanced photocatalytic performance toward decontamination of organic pollutants. *Appl. Surf. Sci.* **2020**, *527*, 146775. [CrossRef]
47. Dou, L.; Li, J.J.; Long, N.; Lai, C.X.; Zhong, J.B.; Li, J.Z.; Huang, S.T. Fabrication of 3D flower-like OVs-Bi_2SiO_5 hierarchical microstructures for visible light-driven removal of tetracycline. *Surf. Interfaces* **2022**, *29*, 101787. [CrossRef]
48. Ye, M.D.; Gong, J.J.; Lai, Y.K.; Lin, C.J.; Lin, Z.Q. High-efficiency photoelectrocatalytic hydrogen generation enabled by palladium quantum dots-sensitized TiO_2 nanotube arrays. *J. Am. Chem. Soc.* **2012**, *134*, 15720–15723. [CrossRef]
49. Chen, P.F.; Chen, L.; Ge, S.F.; Zhang, W.Q.; Wu, M.F.; Xing, P.X.; Rotamond, T.B.; Lin, H.J.; Wu, Y.; He, Y.M. Microwave heating preparation of phosphorus doped g-C_3N_4 and its enhanced performance for photocatalytic H_2 evolution in the help of Ag_3PO_4 nanoparticles. *Int. J. Hydrogen Energ.* **2020**, *45*, 14354–14367. [CrossRef]
50. Zhang, Z.H.; Yu, Y.J.; Wang, P. Hierarchical top-porous/bottom-tubular TiO_2 nanostructures decorated with Pd nanoparticles for efficient photoelectrocatalytic decomposition of synergistic pollutants. *ACS Appl. Mater. Inter.* **2012**, *4*, 990–996. [CrossRef]
51. Ding, Y.Y.; Zhang, J.Y.; Yang, Y.; Long, L.Z.; Yang, L.; Yan, L.J.; Kong, W.J.; Liu, F.C.; Lv, F.Z.; Liu, J. Fully-depleted dual p-n heterojunction with type-II band alignment and matched build-in electric field for high-efficient photocatalytic hydrogen production. *Int. J. Hydrogen Energ.* **2021**, *46*, 36069–36079. [CrossRef]
52. Wang, J.M.; Kuo, M.T.; Zeng, P.; Xu, L.; Chen, S.T.; Peng, T.Y. Few-layer $BiVO_4$ nanosheets decorated with $SrTiO_3$: Rh nanoparticles for highly efficient visible-light-driven overall water splitting. *Appl. Catal. B Environ.* **2020**, *279*, 119377. [CrossRef]
53. Zhou, W.J.; Jia, J.; Lu, J.; Yang, L.J.; Hou, D.M.; Li, G.Q.; Chen, S.W. Recent developments of carbon-based electrocatalysts for hydrogen evolution reaction. *Nano Energy* **2016**, *28*, 29–43. [CrossRef]
54. Wang, Y.; Gao, P.; Li, B.H.; Yin, Z.; Feng, L.; Liu, Y.Z.; Du, Z.W.; Zhang, L.Q. Enhanced photocatalytic performance of visible-light-driven CuO_x/TiO_{2-x} for degradation of gaseous formaldehyde: Roles of oxygen vacancies and nano copper oxides. *Chemosphere* **2022**, *291*, 133007. [CrossRef]
55. Sun, S.M.; Watanabe, M.; Wu, J.; An, Q.; Ishihara, T. Ultrathin $WO_3 \cdot 0.33H_2O$ nanotubes for CO_2 photoreduction to acetate with high selectivity. *J. Am. Chem. Soc.* **2018**, *140*, 6474–6482. [CrossRef]
56. He, W.; Liu, L.; Ma, T.T.; Han, H.M.; Zhu, J.J.; Liu, Y.P.; Fang, Z.; Yang, Z.; Guo, K. Controllable morphology $CoFe_2O_4$/g-C_3N_4 p-n heterojunction photocatalysts with built-in electric field enhance photocatalytic performance. *Appl. Catal. B-Environ.* **2022**, *306*, 121107. [CrossRef]

57. Tahir, M. La-modified TiO_2/carbon nanotubes assembly nanocomposite for efficient photocatalytic hydrogen evolution from glycerol-water mixture. *Int. J. Hydrogen Energy* **2019**, *44*, 3711–3725. [CrossRef]
58. Dubnová, L.; Zvolská, M.; Edelmannová, M.; Matějová, L.; Reli, M.; Drobná, H.; Kuśtrowski, P.; Kočí, K.; Čapek, L. Photocatalytic decomposition of methanol-water solution over N-La/TiO_2 photocatalysts. *Appl. Surf. Sci.* **2019**, *469*, 879–886. [CrossRef]
59. Ye, L.Q.; Liu, J.Y.; Gong, C.Q.; Tian, L.H.; Peng, T.Y.; Zan, L. Two different roles of metallic Ag on Ag/Ag_X/BiO_X (X = Cl, Br) visible light photocatalysts: Surface plasmon resonance and Z-scheme bridge. *ACS Catal.* **2012**, *2*, 1677–1683. [CrossRef]
60. He, Y.M.; Zhang, L.H.; Teng, B.T.; Fan, M.H. A new application of Z-scheme Ag_3PO_4/g-C_3N_4 composite in converting CO_2 to fuel. *Environ. Sci. Technol.* **2015**, *49*, 649–656. [CrossRef]
61. Mohammadi, R.; Massoumi, B. Sn/Cu-TiO_2 nanoparticles produced via sol-gel method: Synthesis, characterization, and photocatalytic activity. *Russ. J. Phys. Chem. A* **2014**, *88*, 1184–1190. [CrossRef]
62. Du, J.M.; Zhao, G.Y.; Pang, H.; Qian, Y.T.; Liu, H.Q.; Kang, D.J. A template method for synthesis of porous Sn-doped TiO_2 monolith and its enhanced photocatalytic activity. *Mater. Lett.* **2013**, *93*, 419–422. [CrossRef]
63. Du, J.M.; Chen, H.J.; Yang, H.; Sang, R.R.; Qian, Y.T.; Li, Y.X.; Zhu, G.G.; Mao, Y.J.; He, W.; Kang, D.J. A facile sol–gel method for synthesis of porous Nd-doped TiO_2 monolith with enhanced photocatalytic activity under UV–vis irradiation. *Micropor. Mesopor. Mat.* **2013**, *182*, 87–94. [CrossRef]
64. Bokare, A.; Pai, M.; Athawale, A.A. Surface modified Nd doped TiO_2 nanoparticles as photocatalysts in UV and solar light irradiation. *Sol. Energy* **2013**, *91*, 111–119. [CrossRef]